



**Magneto-optical conductivity of a topological nodal ring semimetal in a tilted magnetic field**Wenye Duan <sup>1,2</sup> Zhongshui Ma,<sup>3,4</sup> and Chao Zhang<sup>1,\*</sup><sup>1</sup>*School of Physics, University of Wollongong, Wollongong, New South Wales 2522, Australia*<sup>2</sup>*School of Science, East China University of Science and Technology, Shanghai 200237, China*<sup>3</sup>*School of Physics, Peking University, Beijing 100871, China*<sup>4</sup>*Collaborative Innovation Center of Quantum Matter, Beijing 100871, China* (Received 19 June 2019; revised 7 October 2020; accepted 22 October 2020; published 13 November 2020)

The frequency-dependent magneto-optical response of a topological nodal ring semimetal in a tilted magnetic field is studied systematically. Because of its specific low-energy band structure, we find that the magneto-optical response is affected qualitatively by both the strength and direction of the magnetic field. In the clean limit under the magnetic field along the ring axis, the magneto-optical response is investigated analytically, and several meaningful features are presented. For large ring radii, we find an unusual series of peaks in the transverse optical conductivity. As the ring axis tilts away from the magnetic field, the optical transitions are broken by the vertical projection of the magnetic field. For small ring radii, there is mixing of resonant peaks. The magneto-optical conductivities are explained by optical transitions between the underlying Landau level structure. The influence of chemical potential on the magneto-optical conductivities has been investigated correspondingly.

DOI: [10.1103/PhysRevB.102.195123](https://doi.org/10.1103/PhysRevB.102.195123)**I. INTRODUCTION**

It is a remarkable advance in contemporary condensed-matter physics that topological phases of matter have been uncovered more than 80 years after the discovery of the band theory of solids [1]. During the past decade topological materials have attracted tremendous attention both theoretically and experimentally [1–3]. Following the extensive investigations of topological insulators with gapped bulk states, recent attention has focused on gapless topological semimetals such as Dirac or Weyl semimetals. In these systems there is a one-to-one correspondence between the low-energy effective theory of crystalline materials and the equations of high-energy particles [4–6]. Recently, many three-dimensional nodal semimetals whose low-energy effective behaviors have no correspondence to the high-energy particle physics have been predicted. As a new type of these “unconventional” semimetals, topological nodal ring semimetals (TNRSMs) have drawn much attention [7–12]. In TNRSMs, the conduction and valence bands cross at a closed ring nonaccidentally; that is, a crossing cannot become a gapped anticrossing by non-symmetry-breaking perturbations. It is found that nodal rings are protected by inversion and time reversal symmetries [9,12,13], by mirror reflection symmetry [9,12,14,15], and by nonsymmorphic symmetries [9,10,12–14].

The nodal ring band structure was proposed theoretically in the investigation of Berry’s phase in metal physics [7]. The spiral nodal line band structure is formed in the bulk when the number of atomic layers increases in topological matter [8]. Since then, many schemes have been proposed via first-principles calculation to realize TNRSMs [10,12].

A number of physical properties related to their unusual low-energy spectrum have been investigated, including magnetic susceptibility [16], quantum oscillations [17–22], Landau quantization [23–25], quantum anomalies [26], Lifshitz transitions [27], and other transport properties [28–36]. Electronic correlations and superconductivity have also been investigated [37–43]. Optical conductivities of clean and dirty TNRSMs have been studied with both isotropic and anisotropic models [44–46]. The effects of tilt and Dupin cyclide Fermi surfaces on the optical conductivity have also been explored numerically [47].

Optical conductivity can reveal important information on the charge dynamics, which is not directly available in DC measurements. Recent works on optical conductivity have provided valuable information on quasicrystals as well as on Dirac and Weyl semimetals [48–50]. The magneto-optical conductivity of a magnetic field along the ring axis with a chemical potential localized at the nodal loop plane displays the signature of TNRSMs [51–53]. On the other hand, for a magnetic field perpendicular to the ring axis, the spectrum changes qualitatively and shows a nearly flat two-dimensional Landau Level (LL) and dispersive LL structure [16,54]. Considering the intrinsically anisotropic nature of TNRSMs and because magneto-optical measurements are an important probing tool, it is expected that rich structures would be shown in the LL spectrum and magneto-optical responses by tuning the tilting angle between the magnetic field and the ring axis.

In this work, we investigate the magneto-optical conductivities of TNRSMs systematically. By the calculations of both the LLs and magneto-optical responses, the qualitatively different features and their dependence on the strength and direction of the magnetic field relative to the ring axis are shown. The influence of a finite chemical potential will be determined. The characteristic features of the magneto-optical

\*czhang@uow.edu.au

conductivities are explained by the optical transitions between the underlying LL structure.

This paper is organized as follows: in Sec. II we describe the low-energy effective model Hamiltonian of TNRSMs and the energy spectra. In Sec. III, the magneto-optical conductivities are calculated using the Kubo formula, and the analytical results in the limit of the ring axis parallel to the magnetic field

are discussed. The results are generalized to any tilting angles between the ring axis and the magnetic field numerically in Sec. IV. A summary of the results is given in Sec. V.

## II. MODEL AND SPECTRUM

We start from a continuum model Hamiltonian of the form [11,44,46,53]

$$H = v_F \tau_x \otimes (\boldsymbol{\sigma} \cdot \mathbf{p}) + b \sin \theta \tau_z \otimes \sigma_x + b \cos \theta \tau_z \otimes \sigma_z, \quad (1)$$

where  $v_F$  is the Fermi velocity,  $\mathbf{p} = (p_x, p_y, p_z)$  is the momentum equal to  $\hbar \mathbf{k}$  [ $\mathbf{k} = (k_x, k_y, k_z)$ ],  $\theta$  is the tilting angle between the ring axis and the  $z$  axis,  $b/\hbar v_F$  is the radius of the nodal ring,  $\boldsymbol{\sigma} = (\sigma_x, \sigma_y, \sigma_z)$  is the Pauli matrices for the true spin, and  $(\tau_x, \tau_y, \tau_z)$  are the Pauli matrices for pseudospins corresponding to, e.g., sublattices or atom orbitals. The eigenvalues of the Hamiltonian in Eq. (1) are found as

$$E_{\lambda s}(\mathbf{k}) = \lambda \sqrt{\hbar^2 v_F^2 (k_x^2 + k_y^2 + k_z^2) + b^2} + \lambda s 2 \hbar v_F b \sqrt{[k_y^2 + (k_x \cos \theta + k_z \sin \theta)^2]}, \quad (2)$$

where  $\lambda = \pm$  for the conduction and valence bands and  $s = \pm$  refers to the two branches shown in Fig. 1(b) with  $k_z = 0$  and  $\theta = 0$ . The zero-energy contour becomes a circle when  $k_z \cos \theta - k_x \sin \theta = 0$  and  $k_y^2 + (k_x \cos \theta + k_z \sin \theta)^2 = (b/\hbar v_F)^2$ . For a finite Fermi energy  $\mu/b = 0.2$ , the toroidal Fermi surface around the nodal ring is shown in Fig. 1(a). Figure 1(b) shows the low-energy spectrum of a TNRSM at  $k_z = 0$  for  $\theta = 0$  without a magnetic field. For the conduction (valence) band, the  $s = +$  ( $-$ ) branch is **V** shaped, and the  $s = -$  ( $+$ ) branch is **W** shaped along the plane cut across the axis  $k_x = k_y = 0$ .

In the presence of a uniform external magnetic field along the  $z$  direction  $\mathbf{B} = \bar{B} \mathbf{e}_z$ , the vector potential is given in the Landau gauge by  $\mathbf{A} = (0, \bar{B}x, 0)$ . Correspondingly, the Hamiltonian (1) reads

$$H = v_F \tau_x \otimes (\boldsymbol{\sigma} \cdot \boldsymbol{\pi}) + b \sin \theta \tau_z \otimes \sigma_x + b \cos \theta \tau_z \otimes \sigma_z, \quad (3)$$

where  $\boldsymbol{\pi} = \mathbf{p} + e\mathbf{A}$ ,  $-e$  is the electron charge ( $e > 0$ ) and we have ignored the effect of external Zeeman splitting. In general  $[\pi_i, \pi_j] = -ie^{ijk} \hbar e \bar{B}_k$ , with  $i, j, k = (x, y, z)$ . Correspondingly, we have  $[\pi_x, \pi_y] = -i\hbar e \bar{B}$ ,  $[\pi_x, \pi_z] = [\pi_y, \pi_z] = 0$ . For convenience, the energy  $E_{n,\lambda,s}(k_z)$  is scaled in units of  $E_0 = \sqrt{2} \hbar v_F / l_0$ ,  $b_0 = b/E_0$ , and  $k_z$  is in units of  $\sqrt{2}/l_0$ , with  $l_0 = \sqrt{\hbar B / e \bar{B}}$  and  $\bar{B} = B[T]$ . We define the raising and

lowering operators

$$a = \frac{l_0}{\sqrt{2B\hbar}} (\pi_x - i\pi_y) \quad (4)$$

and

$$a^\dagger = \frac{l_0}{\sqrt{2B\hbar}} (\pi_x + i\pi_y), \quad (5)$$

with  $[a, a^\dagger] = 1$ ,  $a|n\rangle = \sqrt{n}|n-1\rangle$ , and  $a^\dagger|n\rangle = \sqrt{n+1}|n+1\rangle$ . The LL wave function is  $\langle \mathbf{r} | n \rangle = i^n (2^n n! \sqrt{\pi} l_0 / \sqrt{B})^{-1/2} e^{-(x-k_y l_0^2/B)^2 / (2l_0^2/B)} H_n[\sqrt{B}(x - k_y l_0^2/B)/l_0]$ , where  $H_n$  is the Hermite polynomial.

The eigenfunctions for the Hamiltonian (3) are found in the form

$$|n, k_y, k_z\rangle = \frac{e^{ik_y y + ik_z z}}{\sqrt{L_y L_z}} \begin{pmatrix} \sum_{n_1} c_{n_1} |n_1 - 1\rangle \\ \sum_{n_2} c_{n_2} |n_2\rangle \\ \sum_{n_3} c_{n_3} |n_3 - 1\rangle \\ \sum_{n_4} c_{n_4} |n_4\rangle \end{pmatrix}. \quad (6)$$

The coefficients in Eq. (6) are determined by the following set of iterative equations:

$$\begin{aligned} b_0 \cos \theta c_{1,n_i} + b_0 \sin \theta c_{2,n_i-1} + k_z c_{3,n_i} + c_{4,n_i} \sqrt{B n_i} &= E c_{1,n_i}, \\ b_0 \sin \theta c_{1,n_i+1} - b_0 \cos \theta c_{2,n_i} + c_{3,n_i} \sqrt{B n_i} - k_z c_{4,n_i} &= E c_{2,n_i}, \\ k_z c_{1,n_i} + c_{2,n_i} \sqrt{B n_i} - b_0 \cos \theta c_{3,n_i} - b_0 \sin \theta c_{4,n_i-1} &= E c_{3,n_i}, \\ c_{1,n_i} \sqrt{B n_i} - k_z c_{2,n_i} - b_0 \sin \theta c_{3,n_i+1} + b_0 \cos \theta c_{4,n_i} &= E c_{4,n_i}. \end{aligned} \quad (7)$$

In order to obtain solutions, a cutoff number  $n_c$  is necessary to truncate the above iterative equations. The cutoff  $n_c$  should be large enough that the low-energy state's properties are not affected by the higher LLs. In our calculations,  $n_c = 30$ . We have numerically checked that this is sufficient in the energy range considered here. As we showed in Ref. [53], the results for  $b_0/\sqrt{B} < 1$  and  $b_0/\sqrt{B} > 1$  are qualitatively different. We shall analyze both cases.

Figure 2 shows the spectra with various tilting angles  $\theta$  for  $b_0 = 0.1$  and 2.5. For  $b_0 = 0.1$ , which satisfies  $b_0/\sqrt{B} < 1$

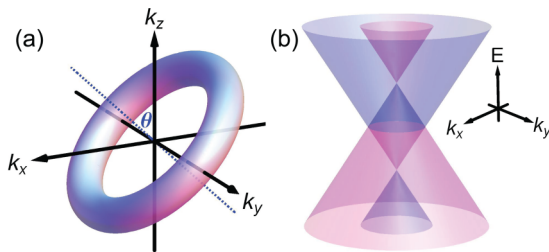


FIG. 1. (a) The toroidal energy surface of a TNRSM at Fermi energy  $\mu/b = 0.2$ . (b) The schematic low-energy spectrum of a TNRSM for  $k_z = 0$  and  $\theta = 0$  without a magnetic field. Light pink shows the  $s = +$  branch, and light blue shows the  $s = -$  branch.

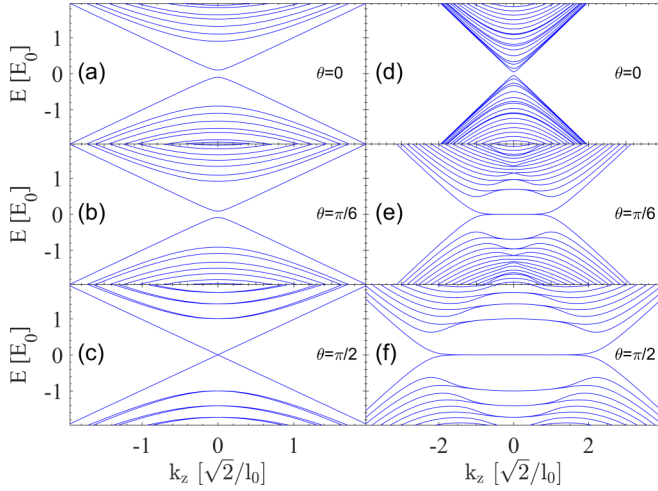


FIG. 2. The spectra in magnetic fields with different tilting angles, (a)–(c)  $b_0 = 0.1$  and (d)–(f)  $b_0 = 2.5$ , with  $B = 1$ .

for  $B = 1$ , it is found that the band gap between the zeroth LLs decreases from  $2b_0$  when the ring axis is parallel to the magnetic field to zero when the ring axis is perpendicular to the magnetic field. The properties are shown in Figs. 2(a)–2(c)

For  $b_0 = 2.5$ , which satisfies  $b_0/\sqrt{B} > 1$  for  $B = 1$ , it is shown that with increasing  $\theta$ , the band gap decreases, and the nearly flat LLs appear. The feature of nearly flat LLs was found in carbon nanotubes [55,56], and similar spectra were also shown in other studies [16,25,54]. At some specific  $k_z$ , the energy bands resemble the spectrum of graphene in  $k_x$ - $k_y$  space. That is, these LLs correspond to the LLs in graphene in this specified nearly flat region of  $k_z$ . In this way, a strong magnetic field perpendicular to the ring axis causes an effective reduction of the dimensionality of the system.

### III. MAGNETO-OPTICAL CONDUCTIVITY IN THE CLEAN LIMIT WITH $\theta = 0$

From the Kubo formula, the optical conductivity is given as

$$\sigma_{ij}(\omega) = \sum_{\alpha, \beta} \frac{-i\hbar[f_F(E_\alpha) - f_F(E_\beta)]\langle\alpha|j_i|\beta\rangle\langle\beta|j_j|\alpha\rangle}{\sqrt{L_x L_y L_z}(E_\alpha - E_\beta)(E_\alpha - E_\beta + \hbar\omega + i\Gamma)}, \quad (8)$$

where  $\alpha, \beta = (n, \lambda, s, k_y, k_z)$ ,  $i, j = (x, y, z)$ ,  $f_F(E_\alpha) = 1/[e^{(E_\alpha - \mu)/T} + 1]$  is the Fermi-Dirac distribution with the chemical potential  $\mu$  at temperature  $T$ ,  $\Gamma$  represents the impurity scattering rate (in this paper, we assume the same  $\Gamma$  for all LLs for simplicity and ignore the exchange-correlation effect), and the current operator  $j_i$  is given by  $j_i = ev_F \tau_x \otimes \sigma_i$ .

Let us first look at the case where the magnetic field is parallel to the ring axis, i.e.,  $\theta = 0$ . The coefficients with  $n_{i\pm 1}$  vanish, and the iterative equations of coefficients with index  $n_i$  are closed in Eq. (7). The eigenstates of Eq. (3) can be solved analytically. The eigenvalues of  $H|n, \lambda, s, k_y, k_z\rangle = E|n, \lambda, s, k_y, k_z\rangle$  are

$$E_{n, \lambda, s}(k_z) = \lambda \sqrt{k_z^2 + (\sqrt{nB} + \lambda s b_0)^2}, \quad (9)$$

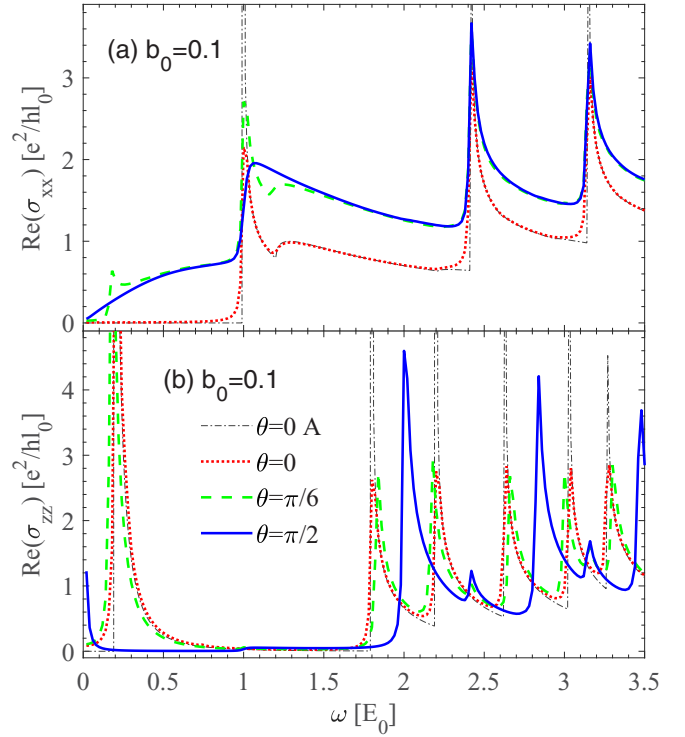


FIG. 3. Plots of (a)  $\text{Re}(\sigma_{xx})$  and (b)  $\text{Re}(\sigma_{zz})$  as a function of the frequency for several different tilting angles. Curve A represents the analytical results in Sec. III. Other parameters are  $\mu = 0$ ,  $T = 0.01$ ,  $B = 1$ , and  $\Gamma = 0.01$ .

where  $\lambda = \pm$ ,  $s = \pm$ , and  $n = 0, 1, 2, \dots$ ; for  $n = 0$ , there is no harm in defining  $s \equiv \lambda$  for convenience. Eigenstates and magneto-optical conductivities are presented in the Appendix. The analytical results of optical conductivities  $\text{Re}(\sigma_{xx})$  and  $\text{Re}(\sigma_{zz})$  are shown as the gray dash-dotted lines in Figs. 3 and 4.

In the clean limit  $\Gamma \rightarrow 0$ , the real part of the optical conductivity is given as

$$\text{Re}[\sigma_{ij}(\omega)] = \sum_{\alpha, \beta} \frac{\pi[f_F(E_\alpha) - f_F(E_\beta)]}{\sqrt{L_x L_y L_z} \omega} \times \langle\alpha|j_i|\beta\rangle\langle\beta|j_j|\alpha\rangle \delta(\hbar\omega + E_\alpha - E_\beta). \quad (10)$$

Both the energy conservation constrained by the  $\delta$  function and the nonvanishing matrix element of the electric current in the above equation determine the selection rules and the transition amplitude. Due to the anisotropic low-energy band structure of the TNRS,  $\text{Re}(\sigma_{xx})$  and  $\text{Re}(\sigma_{zz})$  show different patterns of transition peaks. As the gray dash-dotted lines show in Figs. 3 and 4, we find that the resonant peaks for both  $\text{Re}(\sigma_{xx})$  and  $\text{Re}(\sigma_{zz})$  correspond to the LL transitions at  $k_z = 0$ . More LLs become involved in the transition process as frequency increases. The density of state (DOS) exhibits an onset frequency as an additional LL becomes available and diverges at  $k_z = 0$ . In Table I, we summarize the interband LL transitions for  $\theta = 0$ ,  $\mu = 0$ , and  $T = 0$  in the clean limit as  $k_z \rightarrow 0$ . The LLs are labeled by  $L_{(n, \lambda, s)}$  at  $k_z = 0$ . For  $k_z \neq 0$ , although  $s = \pm$  is still a good band index, the LLs are in mixed states of  $s = +$  and  $s = -$  due to the strong coupling

TABLE I. The interband LL transitions for  $\theta = 0$ ,  $\mu = 0$ , and  $T = 0$  in the clean limit at  $k_z \rightarrow 0$ .

	$b_0$	Transitions	Peak position	Matrix element of the electric current of the order in $k_z$	Peak strength
$\text{Re}(\sigma_{xx})$	$0 < b_0 < \sqrt{nB}$	$L_{(n/n+1,-,-s)} \rightarrow L_{(n+1/n,+,s)}$	$\sqrt{nB} + \sqrt{(n+1)B} + 2sb_0$	$k_z^2$	weak
		$L_{(n/n+1,-,s)} \rightarrow L_{(n+1/n,+,s)}$	$\sqrt{nB} + \sqrt{(n+1)B}$	1	strong
	$\sqrt{nB} \leq b_0 \leq \sqrt{(n+1)B}$	$L_{(n/n+1,-,-)} \rightarrow L_{(n+1/n,+,+)}$	$\sqrt{nB} + \sqrt{(n+1)B} + 2b_0$	$k_z^2$	weak
		$L_{(n/n+1,-,-/+)} \rightarrow L_{(n+1/n,+,+/-)}$	$\sqrt{nB} + \sqrt{(n+1)B}$	1	strong
		$L_{(n/n+1,-,+/-)} \rightarrow L_{(n+1/n,+,+/-)}$	$2b_0 - \sqrt{nB} + \sqrt{(n+1)B}$	$k_z^2$	weak
		$L_{(n/n+1,-,+)} \rightarrow L_{(n+1/n,+,+)}$	$\sqrt{(n+1)B} - \sqrt{nB}$	1	strong
	$\sqrt{(n+1)B} < b_0$	$L_{(n/n+1,-,-s)} \rightarrow L_{(n+1/n,+,s)}$	$2b_0 + s[\sqrt{nB} + \sqrt{(n+1)B}]$	$k_z^2$	weak
		$L_{(n,-,s)} \rightarrow L_{(n+1,+,s)}$	$2b_0 + s[\sqrt{(n+1)B} - \sqrt{nB}]$	$k_z^2$	weak
		$L_{(n+1,-,s)} \rightarrow L_{(n,+,s)}$	$2b_0 + s[\sqrt{nB} - \sqrt{(n+1)B}]$	$k_z^2$	weak
		$L_{(n,-,s)} \rightarrow L_{(n,+,s)}$	$2 \sqrt{nB} + sb_0 $	1	strong

between isospins  $\sigma$  and  $\tau$ . This leads to a mixing of different isospin components in the wave functions.

For  $\sqrt{nB} < b_0$ , the ordering of LLs in the  $s = -$  ( $+$ ) branch of the conduction (valence) band is reversed, and energy decreases with increasing  $n$ . As  $n$  increases further and  $\sqrt{nB} > b_0$ , the LLs resume normal ordering. On the other hand, optical transitions involved in  $\text{Re}(\sigma_{xx})$  are  $L_{(n/n+1,-,s')} \rightarrow L_{(n+1/n,+,s)}$ . Therefore,  $\text{Re}(\sigma_{xx})$  show different features at  $k_z \rightarrow 0$  in three regions, as shown in Table I. We will analyze the characteristics of  $\text{Re}(\sigma_{xx})$  by considering the relative magnitude of  $b_0$  and  $\sqrt{nB}$ .

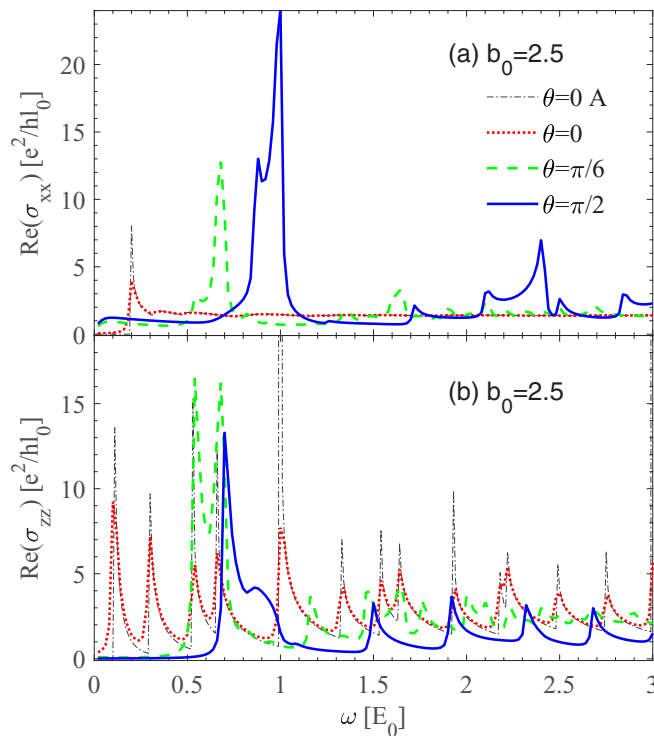


FIG. 4. Plots of (a)  $\text{Re}(\sigma_{xx})$  and (b)  $\text{Re}(\sigma_{zz})$  as a function of the frequency for several different tilting angles. Curve A represents the analytical results in Sec. III. Other parameters are the same as in Fig. 3.

In the case with  $0 < b_0 < \sqrt{nB}$ , all the LLs are normally ordered. For  $s' = s$ , the allowed transitions  $L_{(n/n+1,-,s)} \rightarrow L_{(n+1/n,+,s)}$  have the onset frequency at  $\omega = \sqrt{(n+1)B} + \sqrt{nB}$ , which is independent of  $b_0$  and  $s$ . Therefore, resonant peaks exhibit the sharp onset shown in Fig. 3(a). As summarized in Table I, the matrix elements of the electric current are zeroth order in  $k_z$  in the limit  $k_z \rightarrow 0$ . Besides these strong peaks, there also exist weak peaks when  $s' = -s$ , indicated by the gray dash-dotted line in Fig. 3(a). The optical transitions  $L_{(n/n+1,-,-s)} \rightarrow L_{(n+1/n,+,s)}$  at  $k_z = 0$  give the onset frequency at  $\omega = \sqrt{(n+1)B} + \sqrt{nB} + 2sb_0$ . However, matrix elements of the electric current vanish in the limit  $k_z \rightarrow 0$ . Therefore, the divergence of the  $\delta$  function in Eq. (10) is counterbalanced by the vanishing matrix elements of the electric current at  $k_z = 0$ . As a result, the optical conductivity exhibits weak peaks at  $\omega = \sqrt{(n+1)B} + \sqrt{nB} + 2sb_0$ . In Fig. 3(a), only the first weak peak is visible, and the weak peaks at higher frequency are not resolved due to the background noise. Our results are consistent with previous studies [51,52]. In the case of the Weyl semimetal, only strong peaks are present [48,49]. These additional weak peaks could be regarded as a distinctive feature of the TNRSM.

In the case with  $\sqrt{nB} \leq b_0 \leq \sqrt{(n+1)B}$ , the zeroth to  $n$ th LLs in the  $s = -$  ( $+$ ) branch of the conduction (valence) band are reverse ordered, and the  $(n+1)$ th LLs onwards are normally ordered. There is an additional strong peak at  $\sqrt{(n+1)B} - \sqrt{nB}$  due to the allowed transition  $L_{(n/n+1,-,+)} \rightarrow L_{(n+1/n,+,+)}$  with  $s' = -s = -$  because of the finite matrix element of the electric current at  $k_z = 0$ . Different from the case with  $0 < b_0 < \sqrt{nB}$ , strong peaks are allowed for  $s' = s$ . There is no such corresponding peak in Dirac and Weyl semimetals.

In the last case,  $\sqrt{(n+1)B} < b_0$ , all LLs involved in the transition are reverse ordered. The conductivity exhibits only weak resonances owing to the vanishing current matrix element. The weak resonance region between  $\sqrt{(n+1)B} - \sqrt{nB}$  and  $\sqrt{(n+1)B} + \sqrt{nB}$  contains information on the difference between the TNRSMs and the Dirac/Weyl semimetals. As the gray dash-dotted line shows in Fig. 4(a), for  $\sqrt{6} < b_0 < \sqrt{7}$ , the strong peak is located at  $\sqrt{7} - \sqrt{6} \approx 0.2$  and is the only strong peak in this frequency range.

As shown above, the resonant frequency obeys a  $\omega \propto \sqrt{B}$  law in both the Dirac and Weyl semimetals. The additional strong peak at  $\sqrt{(n+1)B} - \sqrt{nB}$  and the secondary peak in the region between  $\sqrt{(n+1)B} - \sqrt{nB}$  and  $\sqrt{(n+1)B} + \sqrt{nB}$  can offer distinctive signatures of  $\text{Re}(\sigma_{xx})$  of TNRSMs.

For  $\text{Re}(\sigma_{zz})$ , the allowed transitions are  $L_{(n,-,-s)} \rightarrow L_{(n,+,-s)}$ .  $\text{Re}(\sigma_{zz})$  shows an additional strong resonance due to the  $n = 0$  LL transition. This resonant frequency of  $\omega = 2b_0$  is independent of the applied magnetic field. At high frequency, double-peak resonances occur at  $\omega = 2|\sqrt{nB} + sb_0|$  due to the transition between  $n > 0$  LLs. This property is consistent with the previous analysis in Ref. [53].

#### IV. MAGNETO-OPTICAL CONDUCTIVITY IN A TILTED MAGNETIC FIELD

Due to the anisotropic nature of the TNRSM, the tilting angle between the ring axis and the magnetic field could have a significant effect on the magneto-optical response. Here we analyze the magneto-optical conductivities of TNRSMs as a function of the frequency and tilting angles. We find that the features in the magneto-optical conductivity can be explained by the underlying LL structure.

##### A. The effect of $b_0$

The numerical results of magneto-optical conductivities  $\text{Re}(\sigma_{xx})$  and  $\text{Re}(\sigma_{zz})$  as a function of the frequency  $\omega$  for several different tilting angles for  $\mu = 0$  are shown in Figs. 3 and 4. Compared to the analytical results in the clean limit  $\Gamma \rightarrow 0$  for  $\theta = 0$ , it is found that the impurity scattering suppresses the resonant peaks. When the magnetic field is parallel to the ring axis, i.e.,  $\theta = 0$ , our results are in good agreement with the analytical results in Refs. [51–53]. As  $\theta$  increases, the LL transitions for  $\theta = 0$  in Table I are broken by the vertical projection of the magnetic field. Additional features in magneto-optical conductivity can be observed.

In the case of  $b_0 = 0.1$ , as  $\theta$  changes from zero to  $\pi/2$ , the spectrum at  $k_z = 0$  changes from  $\lambda|\sqrt{nB} + \lambda sb_0|$  to  $\lambda\sqrt{nB}$ . The longitudinal and transverse conductivities at nonzero  $\theta$  show a mixture of  $\text{Re}(\sigma_{xx})$  and  $\text{Re}(\sigma_{zz})$  at  $\theta = 0$ . The evolution of the LLs with  $\theta$  and the mixture of the conductivities induce the following features: for  $\text{Re}(\sigma_{xx})$ , an additional mixed peak emerges at low energy, and the sharp peak at  $\omega = 1$  changes to a smooth absorption shoulder as  $\theta$  increases. The positions of the strong peaks at  $\sqrt{nB} + \sqrt{(n+1)B}$  are not affected by  $\theta$  because they are independent of the band gap of the lowest LLs and the split gaps of the higher LLs. The characteristic weak peak of  $\text{Re}(\sigma_{xx})$  [51,52] fades away, as shown in Fig. 3(a). For  $\text{Re}(\sigma_{zz})$ , the position of the lowest resonant energy is no longer at  $2b_0$  but shifts to zero. The characteristic high LL double peaks at  $2|\sqrt{nB} + \lambda sb_0|$  [53] merge together at  $2\sqrt{nB}$ . There are additional mixed peaks at the corresponding higher LL peak positions  $\sqrt{nB} + \sqrt{(n+1)B}$  of  $\text{Re}(\sigma_{xx})$ , as shown in Fig. 3(b).

In the case of  $b_0 = 2.5$ , as  $\theta$  increases, the reverse-ordered low-energy LLs become nearly flat. The nearly flat LLs at  $k_z = 0$  tend to  $\lambda\sqrt{nB}$  as  $\theta$  approaches  $\pi/2$ . For  $\text{Re}(\sigma_{xx})$ , the additional strong peak at  $\sqrt{(n+1)B} - \sqrt{nB}$  due to the transition between the reversed  $s = -$  branch disappears. On

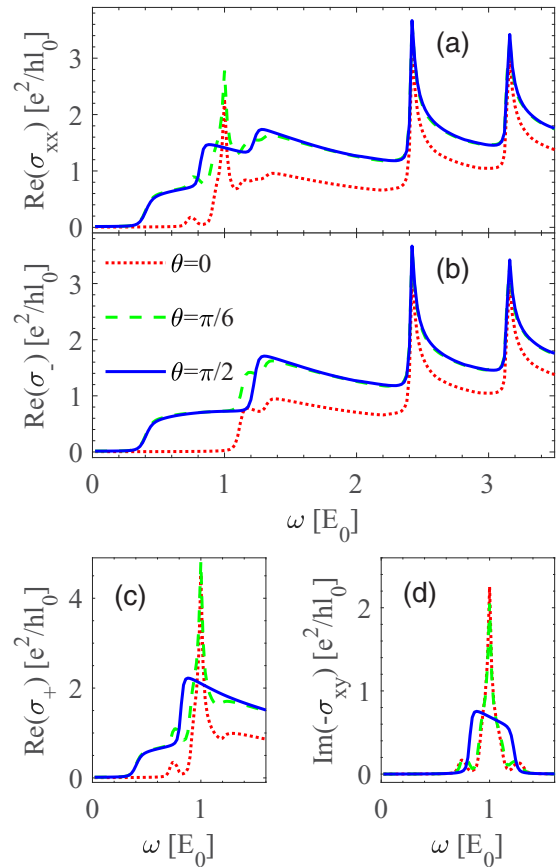


FIG. 5. Plots of (a)  $\text{Re}(\sigma_{xx})$ , (b)  $\text{Re}(\sigma_-)$ , (c)  $\text{Re}(\sigma_+)$ , and (d)  $\text{Im}(-\sigma_{xy})$  as a function of the frequency for several different tilting angles for  $b_0 = 0.1$ . Other parameters are  $\mu = 0.2$ ,  $T = 0.01$ ,  $B = 1$ , and  $\Gamma = 0.01$ .

the other hand, a series of asymmetric resonant peaks with a sharp onset appears due to transitions between discrete dispersive LLs. Furthermore, a series of asymmetric resonant peaks with a slow onset and sharp falling edge appears due to transitions between nearly flat LLs in the region between  $\sqrt{(n+1)B} - \sqrt{nB}$  and  $\sqrt{(n+1)B} + \sqrt{nB}$ . The tilting angle modifies the three-dimensional dispersive LL structure and hence the magneto-optical conductivities. The amplitude of the peak with a slow onset and fast decay increases because of the enhanced DOS of the nearly flat LLs, and their locations are dependent on the band gap of the nearly flat LLs. For  $\text{Re}(\sigma_{zz})$ , as shown in Fig. 4(b), when  $\theta = \pi/2$ , only the resonant peaks with a sharp onset remain. The mixing of  $\text{Re}(\sigma_{xx})$  and  $\text{Re}(\sigma_{zz})$  is not shown. The analysis here indicates the dependence of the longitudinal and transverse conductivities on  $\theta$  is determined by the ratio of  $b_0/\sqrt{B}$ .

##### B. The effect of finite chemical potential

The magneto-optical conductivity is sensitive to changing the chemical potential. Due to the particle-hole symmetry, we will consider only the  $\mu > 0$  case. In Figs. 5 and 6, the optical conductivities with chemical potential  $\mu = 0.2$  are depicted.

As shown in Fig. 5(a), new resonant peaks appear at a finite chemical potential for  $b_0 = 0.1$ . For  $\theta = 0$ , the

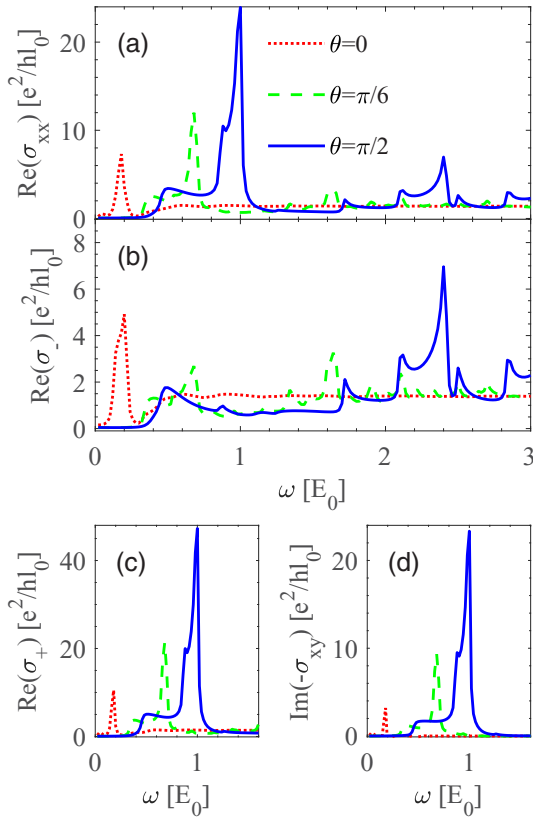


FIG. 6. Plots of (a)  $\text{Re}(\sigma_{xx})$ , (b)  $\text{Re}(\sigma_-)$ , (c)  $\text{Re}(\sigma_+)$ , and (d)  $\text{Im}(-\sigma_{xy})$  as a function of the frequency for several different tilting angles for  $b_0 = 2.5$ . Other parameters are the same as in Fig. 5.

additional low-energy peak is induced by the intraband transition  $L_{(0,+)} \rightarrow L_{(1,+)}$ . Two broad peaks for  $1 < \omega < 1 + 2\mu$  are due to the interband transitions  $L_{(1,-)} \rightarrow L_{(0,+)}$ . The peaks in the high-frequency region  $\omega \gtrsim 1 + 2\mu$  are unaffected. Increasing  $\theta$  to  $\pi/2$ , as the band gap of the lowest LLs and the split gaps of the higher LLs decrease, the resonant peaks merge to two shoulder peaks and an absorption edge at a low frequency  $\omega \approx 2\mu$ .

At  $\mu = 0$ , because of the particle-hole symmetry  $\text{Im}(-\sigma_{xy})$  is zero in the whole frequency region. At a finite chemical potential  $\mu > 0$ ,  $\text{Im}(-\sigma_{xy})$  is finite due to the absence of the particle-hole symmetry. The peak pattern has an origin similar to that of  $\text{Re}(\sigma_{xx})$  in the frequency region  $1 - 2\mu < \omega < 1 + 2\mu$ . As  $\theta$  increases, the strong peak and two weak peaks at  $\theta = 0$  merge into one broad peak at  $\theta = \pi/2$ .

So far we have investigated  $\text{Re}(\sigma_{xx})$  and  $\text{Im}(-\sigma_{xy})$ . In experiments involving polarized light, such as the Faraday and Kerr effects, the magnetic-optical response to the right- and left-handed polarized light  $\sigma_{\pm} = \sigma_{xx} \pm i\sigma_{xy}$  is more relevant. The absorptive part of  $\sigma_{\pm}$  is  $\text{Re}(\sigma_{\pm}) = \text{Re}(\sigma_{xx}) \mp \text{Im}(\sigma_{xy})$ , shown in Figs. 5(b) and 5(c). Because of the cancellation of  $\text{Im}(-\sigma_{xy})$  and  $\text{Re}(\sigma_{xx})$ ,  $\text{Re}(\sigma_-)$  shows smooth weak peaks in the region  $1 < \omega < 1 + 2\mu$ . On the other hand, because of the superposition of  $\text{Im}(-\sigma_{xy})$  and  $\text{Re}(\sigma_{xx})$ , the peak magnitude of  $\text{Re}(\sigma_+)$  is enhanced, as shown in Fig. 5(c). This feature resembles that of Weyl semimetals [48].

The influence of the finite chemical potential on the optical conductivity for  $b_0 = 2.5$  is shown in Fig. 6. The spectral weight of the strong intraband peak of  $\text{Re}(\sigma_{xx})$  at  $\theta = 0$  is redistributed among the interband peaks and additional shoulders as  $\theta$  increases, as shown in Fig. 6(a).

The Hall conductivity  $\text{Im}(-\sigma_{xy})$  at  $\mu = 0.2$  is shown in Fig. 6(d). Distinct from  $b_0 = 0.1$ , as  $\theta$  increases, the strong peak of  $\text{Im}(-\sigma_{xy})$  increases due to the contribution from the nearly flat LLs. The peak position is affected by  $\theta$  because of the increasing gap of the nearly flat LLs with increasing  $\theta$ .  $\text{Re}(\sigma_+)$  and  $\text{Re}(\sigma_-)$  for  $b_0 = 2.5$  show a  $\mu$  dependence similar to that for  $b_0 = 0.1$ .

## V. SUMMARY AND DISCUSSION

In summary, we have performed a systematic study on the magneto-optical conductivity of a TNRSM. The influence of both the strength and direction of the magnetic field relative to the ring axis on the optical conductivities was investigated. The magneto-optical response exhibits characteristics related to the specific low-energy properties of nodal rings. In the clean limit of the ring axis parallel to the magnetic field with  $\mu = 0$ , the interband LL transitions are dependent on the relative magnitude of  $b_0$  to  $\sqrt{B}$ . In the case  $\sqrt{nB} \leq b_0 \leq \sqrt{(n+1)B}$ , we find that there is an additional strong peak at  $\sqrt{(n+1)B} - \sqrt{nB}$  in  $\text{Re}(\sigma_{xx})$  due to the reverse-ordered LL. Besides, there are only weak peaks in the frequency region between  $\sqrt{(n+1)B} - \sqrt{nB}$  and  $\sqrt{(n+1)B} + \sqrt{nB}$ . The distinctive weak peaks in  $\text{Re}(\sigma_{xx})$  in the case of  $0 < b_0 < \sqrt{nB}$  are too vague to resolve in magneto-infrared spectroscopy experiments [51]. However, this additional strong peak represents an observable signature of TNRSMs in magneto-infrared spectroscopy experiments.

Increasing the tilting angle  $\theta$ , for  $b_0 = 0.1$ , the band gap of the lowest LLs and the split of higher LLs decrease. There is a mixing of  $\text{Re}(\sigma_{xx})$  and  $\text{Re}(\sigma_{zz})$  of  $\theta = 0$ . For  $b_0 = 2.5$ , the magnetic field component perpendicular to the ring axis causes an effective reduction in the dimensionality of the system. Therefore, the band gap closes, and nearly flat LLs appear around  $k_z = 0$ . As a result, the optical transitions between the nearly flat LLs show strong peaks with a slow onset and sharp decrease. On the other hand, the resonant peaks due to dispersive LLs exhibit a sharp onset and a slow decrease.

In addition, at a finite chemical potential, the conductivities for left- and right-hand circularly polarized light behave differently. The origin of these distinctive features is explained by the underlying LL structure.

Finally, we would like to make a remark on the effective linear model used in our study. The effective linear model is valid in an energy window of more than 200 meV, i.e.,  $(-100 \text{ meV}, 100 \text{ meV})$ , as confirmed in Fig. 4 of Ref. [57] and Table 7 of Ref. [12]. Considering the Fermi velocity is of the order of  $10^5 \text{ m s}^{-1}$ , it can be estimated that the frequency regime discussed in this paper is less than  $\omega < 4E_0 \sim 14.4 \text{ meV}$ . These transition energies are very low and well within the valid regime of the linear energy dispersion. Therefore, our results remain accurate in this frequency regime. In addition, if we consider the model with anisotropic Fermi

velocities corresponding to ellipsoidal nodal curves,

$$H = \tau_x \otimes \left( \sum_{i=x,y,z} v_i \sigma_i p_i \right) + b \tau_z \otimes \sigma_z, \quad (11)$$

the corresponding Hamiltonian in a magnetic field is

$$H = v_F \tau_x \otimes \left( \sum_{i=x,y,z} a_i \sigma_i \pi_i \right) + b \tau_z \otimes \sigma_z, \quad (12)$$

where  $v_F = (v_x v_y v_z)^{1/3}$  and  $a_i = v_i / v_F$ . This anisotropic model can be mapped to the isotropic model (i.e., the ring model in our study) by rescaling the three axes  $p'_i = a_i p_i$  and  $r'_i = r_i / a_i$ . The Hamiltonian becomes

$$H = v_F \tau_x \otimes (\boldsymbol{\sigma} \cdot \boldsymbol{\pi}') + b \tau_z \otimes \sigma_z. \quad (13)$$

Hence, the results presented in our work by the low-energy effective model and in other studies of transport properties [16,44,46,51,54] can be directly applied. It should be noted that there exists a different type of TNRSM which is described by a two-band model  $H = \frac{\hbar^2}{2m}(k_x^2 + k_y^2 - b^2)\tau_x + \hbar v_F k_z \tau_z$  [9,14,58]. In this nodal ring system, the region of linear dispersion is narrow. Its magnetic-optical response has not been reported yet.

#### ACKNOWLEDGMENTS

This work is supported by the Australian Research Council (Grant No. DP160101474), NSFC (Grant No. 11774006), and NBRP of China (Grant No. 2012CB921300). We would like to thank J. Zuber for his critical reading of the manuscript and his assistance in improving the English.

#### APPENDIX

The eigenstates are

$$|n, \lambda, s, k_y, k_z\rangle = \frac{\frac{e^{iky+ik_zz}}{\sqrt{L_y L_z}} c_n}{\sqrt{k_z^2 + (\sqrt{nB} + \lambda s b_0 - \lambda s E_{n,\lambda,s})^2}} \begin{pmatrix} \lambda s k_z |n-1\rangle \\ \lambda s (\sqrt{nB} + \lambda s b_0 - \lambda s E_{n,\lambda,s}) |n\rangle \\ -(\sqrt{nB} + \lambda s b_0 - \lambda s E_{n,\lambda,s}) |n-1\rangle \\ k_z |n\rangle \end{pmatrix}, \quad (A1)$$

where

$$c_n = \begin{cases} 1 & n = 0, \\ \frac{1}{\sqrt{2}} & n > 0. \end{cases}$$

By the Kubo formula, we obtain the following conductivities in the clean limit  $\Gamma \rightarrow 0$ :

$$\begin{aligned} \text{Re}[\sigma_{xx}(\omega)] &= \frac{\sqrt{2} B e^2}{\hbar l_0} \sum_{n,\lambda,\lambda',s,s'} \frac{c_n^2 c_{n+1}^2}{\tilde{\omega}} \left\{ [f_F(E_{n+1,\lambda,s}) - f_F(E_{n,\lambda',s'})] \left| \frac{E_{n,\lambda',s'} E_{n+1,\lambda,s}}{k_{z,n,\lambda,\lambda',s,s'} \tilde{\omega}} \right| \right. \\ &\times \frac{[\lambda s k_{z,n,\lambda,\lambda',s,s'}^2 - \lambda' s' (\sqrt{(n+1)B} + \lambda s b_0 - \lambda s E_{n+1,\lambda,s}) (\sqrt{nB} + \lambda' s' b_0 - \lambda' s' E_{n,\lambda',s'})]^2}{[k_{z,n,\lambda,\lambda',s,s'}^2 + (\sqrt{nB} + \lambda' s' b_0 - \lambda' s' E_{n,\lambda',s'})^2] [k_{z,n,\lambda,\lambda',s,s'}^2 + (\sqrt{(n+1)B} + \lambda s b_0 - \lambda s E_{n+1,\lambda,s})^2]} \\ &+ [f_F(E_{n,\lambda,s}) - f_F(E_{n+1,\lambda',s'})] \left| \frac{E_{n+1,\lambda',s'} E_{n,\lambda,s}}{k_{z,n,\lambda,\lambda',s,s'} \tilde{\omega}} \right| \\ &\times \left. \frac{[\lambda' s' k_{z,n,\lambda,\lambda',s,s'}^2 - \lambda s (\sqrt{nB} + \lambda s b_0 - \lambda s E_{n,\lambda,s}) (\sqrt{(n+1)B} + \lambda' s' b_0 - \lambda' s' E_{n+1,\lambda',s'})]^2}{[k_{z,n,\lambda,\lambda',s,s'}^2 + (\sqrt{(n+1)B} + \lambda' s' b_0 - \lambda' s' E_{n+1,\lambda',s'})^2] [k_{z,n,\lambda,\lambda',s,s'}^2 + (\sqrt{nB} + \lambda s b_0 - \lambda s E_{n,\lambda,s})^2]} \right\}, \quad (A2) \end{aligned}$$

$$\begin{aligned} \text{Im}[\sigma_{xy}(\omega)] &= \frac{\sqrt{2} B e^2}{\hbar l_0} \sum_{n,\lambda,\lambda',s,s'} \frac{c_n^2 c_{n+1}^2}{\tilde{\omega}} \left\{ [f_F(E_{n+1,\lambda,s}) - f_F(E_{n,\lambda',s'})] \left| \frac{E_{n,\lambda',s'} E_{n+1,\lambda,s}}{k_{z,n,\lambda,\lambda',s,s'} \tilde{\omega}} \right| \right. \\ &\times \frac{[\lambda s k_{z,n,\lambda,\lambda',s,s'}^2 - \lambda' s' (\sqrt{(n+1)B} + \lambda s b_0 - \lambda s E_{n+1,\lambda,s}) (\sqrt{nB} + \lambda' s' b_0 - \lambda' s' E_{n,\lambda',s'})]^2}{[k_{z,n,\lambda,\lambda',s,s'}^2 + (\sqrt{nB} + \lambda' s' b_0 - \lambda' s' E_{n,\lambda',s'})^2] [k_{z,n,\lambda,\lambda',s,s'}^2 + (\sqrt{(n+1)B} + \lambda s b_0 - \lambda s E_{n+1,\lambda,s})^2]} \\ &- [f_F(E_{n,\lambda,s}) - f_F(E_{n+1,\lambda',s'})] \left| \frac{E_{n+1,\lambda',s'} E_{n,\lambda,s}}{k_{z,n,\lambda,\lambda',s,s'} \tilde{\omega}} \right| \\ &\times \left. \frac{[\lambda' s' k_{z,n,\lambda,\lambda',s,s'}^2 - \lambda s (\sqrt{nB} + \lambda s b_0 - \lambda s E_{n,\lambda,s}) (\sqrt{(n+1)B} + \lambda' s' b_0 - \lambda' s' E_{n+1,\lambda',s'})]^2}{[k_{z,n,\lambda,\lambda',s,s'}^2 + (\sqrt{(n+1)B} + \lambda' s' b_0 - \lambda' s' E_{n+1,\lambda',s'})^2] [k_{z,n,\lambda,\lambda',s,s'}^2 + (\sqrt{nB} + \lambda s b_0 - \lambda s E_{n,\lambda,s})^2]} \right\}, \quad (A3) \end{aligned}$$

where  $\tilde{\omega} = \omega/E_0$

$$k_{z,n,\lambda,\lambda',s,s'} = \frac{\sqrt{(8b_0^2 - 4\tilde{\omega}^2)nB + (\tilde{\omega}^2 - 1)(\tilde{\omega}^2 - 1 - 4b_0^2 - \lambda s 4b_0\sqrt{(1+n)B}) - \lambda's'4b_0\sqrt{nB}(1 + \tilde{\omega}^2 + \lambda s 2b_0\sqrt{(1+n)B})}}{2\tilde{\omega}}$$

and

$$\begin{aligned} \text{Re}[\sigma_{zz}(\omega)] &= \frac{2\sqrt{2}Be^2}{\hbar l_0} \sum_{n,\lambda,\lambda',s,s'} c_n^4 \frac{f_F(E_{n,\lambda,s}) - f_F(E_{n,\lambda',s'})}{\tilde{\omega}} \left| \frac{k_{z,n,\lambda,\lambda',s,s'} E_{n,\lambda,s} E_{n,\lambda',s'}}{\tilde{\omega}} \right| (\lambda s \lambda' s' + 1) \\ &\times \frac{[\lambda s(\sqrt{nB} + \lambda s b_0 - \lambda s E_{n,\lambda,s}) + \lambda' s'(\sqrt{nB} + \lambda' s' b_0 - \lambda' s' E_{n,\lambda',s'})]^2}{[k_{z,n,\lambda,\lambda',s,s'}^2 + (\sqrt{nB} + \lambda' s' b_0 - \lambda' s' E_{n,\lambda',s'})^2][k_{z,n,\lambda,\lambda',s,s'}^2 + (\sqrt{nB} + \lambda s b_0 - \lambda s E_{n,\lambda,s})^2]}, \end{aligned} \quad (\text{A4})$$

where for  $\lambda' = -\lambda$  and  $s' = -s$ ,  $k_{z,n,\lambda,\lambda',s,s'} = \frac{1}{2}\sqrt{\tilde{\omega}^2 - 4(b_0 + \lambda s\sqrt{nB})^2}$ .

- 
- [1] M. Z. Hasan and C. L. Kane, *Rev. Mod. Phys.* **82**, 3045 (2010).  
[2] X.-L. Qi and S.-C. Zhang, *Rev. Mod. Phys.* **83**, 1057 (2011).  
[3] C.-K. Chiu, J. C. Y. Teo, A. P. Schnyder, and S. Ryu, *Rev. Mod. Phys.* **88**, 035005 (2016).  
[4] M. Z. Hasan, S.-Y. Xu, I. Belopolski, and S.-M. Huang, *Annu. Rev. Condens. Matter Phys.* **8**, 289 (2017).  
[5] B. Yan and C. Felser, *Annu. Rev. Condens. Matter Phys.* **8**, 337 (2017).  
[6] N. P. Armitage, E. J. Mele, and A. Vishwanath, *Rev. Mod. Phys.* **90**, 015001 (2018).  
[7] G. P. Mikitik and Y. V. Sharlai, *Phys. Rev. Lett.* **82**, 2147 (1999).  
[8] T. T. Heikkilä and G. E. Volovik, *JETP Lett.* **93**, 59 (2011).  
[9] C. Fang, H. Weng, X. Dai, and Z. Fang, *Chin. Phys. B* **25**, 117106 (2016).  
[10] R. Yu, Z. Fang, X. Dai, and H. Weng, *Front. Phys.* **12**, 127202 (2017).  
[11] A. A. Burkov, M. D. Hook, and L. Balents, *Phys. Rev. B* **84**, 235126 (2011).  
[12] S.-Y. Yang, H. Yang, E. Derunova, S. S. P. Parkin, B. Yan, and M. N. Ali, *Adv. Phys.: X* **3**, 1414631 (2018).  
[13] Y. Kim, B. J. Wieder, C. L. Kane, and A. M. Rappe, *Phys. Rev. Lett.* **115**, 036806 (2015).  
[14] C. Fang, Y. Chen, H.-Y. Kee, and L. Fu, *Phys. Rev. B* **92**, 081201(R) (2015).  
[15] Y.-H. Chan, C.-K. Chiu, M. Y. Chou, and A. P. Schnyder, *Phys. Rev. B* **93**, 205132 (2016).  
[16] M. Koshino and I. F. Hizbullah, *Phys. Rev. B* **93**, 045201 (2016).  
[17] C. Li, C. M. Wang, B. Wan, X. Wan, H.-Z. Lu, and X. C. Xie, *Phys. Rev. Lett.* **120**, 146602 (2018).  
[18] H. Yang, R. Moessner, and L.-K. Lim, *Phys. Rev. B* **97**, 165118 (2018).  
[19] M. R. van Delft, S. Pezzini, T. Khouri, C. S. A. Müller, M. Breitzkreuz, L. M. Schoop, A. Carrington, N. E. Hussey, and S. Wiedmann, *Phys. Rev. Lett.* **121**, 256602 (2018).  
[20] S. Li, Z. Guo, D. Fu, X.-C. Pan, J. Wang, K. Ran, S. Bao, Z. Ma, Z. Cai, R. Wang, R. Yu, J. Sun, F. Song, and J. Wen, *Sci. Bull.* **63**, 535 (2018).  
[21] J. Hu, Z. Tang, J. Liu, X. Liu, Y. Zhu, D. Graf, K. Myhro, S. Tran, C. N. Lau, J. Wei, and Z. Mao, *Phys. Rev. Lett.* **117**, 016602 (2016).  
[22] L. Oroszlány, B. Dóra, J. Cserti, and A. Cortijo, *Phys. Rev. B* **97**, 205107 (2018).  
[23] J.-W. Rhim and Y. B. Kim, *Phys. Rev. B* **92**, 045126 (2015).  
[24] K. Mullen, B. Uchoa, and D. T. Glatzhofer, *Phys. Rev. Lett.* **115**, 026403 (2015).  
[25] H. Yao, M. Zhu, L. Jiang, and Y. Zheng, *J. Phys.: Condens. Matter* **30**, 285501 (2018).  
[26] A. A. Burkov, *Phys. Rev. B* **97**, 165104 (2018).  
[27] H. Jiang, L. Li, J. Gong, and S. Chen, *Eur. Phys. J. B* **91**, 75 (2018).  
[28] W. Chen, K. Luo, L. Li, and O. Zilberberg, *Phys. Rev. Lett.* **121**, 166802 (2018).  
[29] S. T. Ramamurthy and T. L. Hughes, *Phys. Rev. B* **95**, 075138 (2017).  
[30] T. Rauch, H. Nguyen Minh, J. Henk, and I. Mertig, *Phys. Rev. B* **96**, 235103 (2017).  
[31] M. Biderang, A. Leonhardt, N. Raghuvanshi, A. P. Schnyder, and A. Akbari, *Phys. Rev. B* **98**, 075115 (2018).  
[32] V. I. Gavrilenko, A. A. Perov, A. P. Protogenov, R. V. Turkevich, and E. V. Chulkov, *Phys. Rev. B* **97**, 115204 (2018).  
[33] W. B. Rui, Y. X. Zhao, and A. P. Schnyder, *Phys. Rev. B* **97**, 161113(R) (2018).  
[34] R. A. Molina and J. González, *Phys. Rev. Lett.* **120**, 146601 (2018).  
[35] D. A. Khokhlov, A. L. Rakhmanov, and A. V. Rozhkov, *Phys. Rev. B* **97**, 235418 (2018).  
[36] Y. Sun, Y. Zhang, C.-X. Liu, C. Felser, and B. Yan, *Phys. Rev. B* **95**, 235104 (2017).  
[37] B. Roy, *Phys. Rev. B* **96**, 041113(R) (2017).  
[38] J. Liu and L. Balents, *Phys. Rev. B* **95**, 075426 (2017).  
[39] A. P. Schnyder and S. Ryu, *Phys. Rev. B* **84**, 060504(R) (2011).  
[40] R. Nandkishore, *Phys. Rev. B* **93**, 020506(R) (2016).  
[41] Y. Wang and R. M. Nandkishore, *Phys. Rev. B* **95**, 060506(R) (2017).  
[42] S. E. Han, G. Y. Cho, and E.-G. Moon, *Phys. Rev. B* **95**, 094502 (2017).  
[43] S. A. Yang, H. Pan, and F. Zhang, *Phys. Rev. Lett.* **113**, 046401 (2014).  
[44] J. P. Carbotte, *J. Phys.: Condens. Matter* **29**, 045301 (2017).  
[45] S. Barati and S. H. Abedinpour, *Phys. Rev. B* **96**, 155150 (2017).  
[46] S. P. Mukherjee and J. P. Carbotte, *Phys. Rev. B* **95**, 214203 (2017).



- [47] S. Ahn, E. J. Mele, and H. Min, *Phys. Rev. Lett.* **119**, 147402 (2017).
- [48] P. E. C. Ashby and J. P. Carbotte, *Phys. Rev. B* **87**, 245131 (2013).
- [49] Y. Sun and A.-M. Wang, *Phys. Rev. B* **96**, 085147 (2017).
- [50] J. D. Malcolm and E. J. Nicol, *Phys. Rev. B* **94**, 224305 (2016).
- [51] R. Y. Chen, Z. G. Chen, X.-Y. Song, J. A. Schneeloch, G. D. Gu, F. Wang, and N. L. Wang, *Phys. Rev. Lett.* **115**, 176404 (2015).
- [52] Y.-X. Wang, *Eur. Phys. J. B* **90**, 99 (2017).
- [53] W. Duan, C. Yang, Z. Ma, Y. Zhu, and C. Zhang, *Phys. Rev. B* **99**, 045124 (2019).
- [54] T. Bzdušek, Q. Wu, A. Rüegg, M. Sigrist, and A. A. Soluyanov, *Nature (London)* **538**, 75 (2016).
- [55] E. Perfetto, J. González, F. Guinea, S. Bellucci, and P. Onorato, *Phys. Rev. B* **76**, 125430 (2007).
- [56] P. Onorato, *Phys. Rev. B* **84**, 233403 (2011).
- [57] M. A. Zeb and H.-Y. Kee, *Phys. Rev. B* **86**, 085149 (2012).
- [58] Z. Yan, P.-W. Huang, and Z. Wang, *Phys. Rev. B* **93**, 085138 (2016).